

Article

Oxalamide Based Fe(II)-MOFs as Potential Electrode Modifiers for Glucose Detection

Panagiotis Oikonomopoulos ¹, Varvara Pagkali ², Evangelia Kritikou ², Anthi Panara ², Marios G. Kostakis ², Nicolaos S. Thomaidis ², Thomais G. Tziotzi ³, Anastasios Economou ², Christos Kokkinos ² and Giannis S. Papaefstathiou ^{1,*}

¹ Laboratory of Inorganic Chemistry, Department of Chemistry, National and Kapodistrian University of Athens, 15771 Athens, Greece

² Laboratory of Analytical Chemistry, Department of Chemistry, National and Kapodistrian University of Athens, 15771 Athens, Greece

³ Department of Chemistry, University of Crete, Voutes, 71003 Herakleion, Greece

* Correspondence: gspapaef@chem.uoa.gr

Abstract: In an attempt to expand the coordination chemistry of N,N'-bis(2,4-dicarboxyphenyl)-oxalamide (H₆L) ligand, we isolated and structurally characterized two new Fe(II) Metal-Organic Frameworks (MOFs), namely [Fe₂(H₂L)(H₂O)₅] (**3D-Fe-MOF**) and [Fe(H₄L)(H₂O)₂]·2H₂O, (**2D-Fe-MOF**) by carefully adjusting the reaction conditions to achieve the optimal degree of deprotonation of the bridging ligand. Both MOFs were found stable in water, as evidenced by powder X-ray diffraction data and their ability to sorb glucose (GLU) from either an aqueous solution or artificial sweat was investigated only to show negligible sorption. A graphite paste sensor (GPE) using the **3D-Fe-MOF** as a modifier was fabricated. The **3D-Fe-MOF** modified GPE was assessed for non-enzymatic GLU detection in aqueous solution at pH 6 via differential pulse voltammetry and the preliminary results were discussed.



Citation: Oikonomopoulos, P.; Pagkali, V.; Kritikou, E.; Panara, A.; Kostakis, M.G.; Thomaidis, N.S.; Tziotzi, T.G.; Economou, A.; Kokkinos, C.; Papaefstathiou, G.S. Oxalamide Based Fe(II)-MOFs as Potential Electrode Modifiers for Glucose Detection. *Chemistry* **2023**, *5*, 19–30. <https://doi.org/10.3390/chemistry5010002>

Academic Editors: Zoi Lada and Konstantis Konidaris

Received: 30 November 2022

Revised: 15 December 2022

Accepted: 16 December 2022

Published: 20 December 2022



Copyright: © 2022 by the authors. Licensee MDPI, Basel, Switzerland. This article is an open access article distributed under the terms and conditions of the Creative Commons Attribution (CC BY) license (<https://creativecommons.org/licenses/by/4.0/>).

Keywords: GLU; iron; metal-organic frameworks; nonenzymatic; voltammetry

1. Introduction

Diabetes mellitus is a serious disease, resulting from the insufficiency of insulin in the body, which causes elevated blood-glucose (GLU) levels (hyperglycemia) or reduced GLU concentrations (hypoglycemia). The continuous monitoring of blood GLU levels in diabetic patients is an important matter, as shown by the development of electrochemical GLU biosensors throughout the last two decades [1,2]. The majority of the electrochemical biosensors, reported in the literature, focus on monitoring the blood GLU levels, which includes the painful and inconvenient process of blood samples for the patients [3]. Nevertheless, more recently, scientists have also turned their interest to sweat sampling and wearable sensors, not only for GLU but for other biomarkers too, thanks to the ease of sampling from the skin surface, as the GLU blood levels are associated with the sweat levels [4–6]. GLU sensors are divided into enzymatic and non-enzymatic ones, with the first ones being based on the presence of enzymes such as GLU oxidase, hexokinase, and GLU dehydrogenase [1,7]. On the other hand, non-enzymatic sensors are broadly adaptable, providing stability, simplicity, and reproducibility, while are not affected by temperature, pH, or humidity [8–10].

The extended research around electrochemical sensors has led to the exploitation of different kinds of electrode modifiers, such as metal oxides, metal compounds, and recently, metal-organic frameworks (MOFs), in either enzymatic or non-enzymatic sensors [2,11,12]. MOFs are crystalline, porous materials composed of metal ions or metal clusters and polytopic bridging organic linkers, demonstrating fascinating properties such as high surface area, thermal stability, tunable pore size [13], and magnetic properties [14]. They have

potential applications in many fields including catalysis, gas storage, energy storage, environmental pollution, sensing platforms, catalysis, photocatalysis, oxidation, hydrogenation, and separation due to their diverse active sites and latterly as electrode modifiers for GLU sensing in blood serum or sweat samples [13,15–21]. In the case of enzymatic sensors, MOFs are usually used as an immobilization matrix for the appropriate enzyme, with the redox abilities of the electrode to be enhanced by the metal centers of the MOFs. Such an example is the case of the HP-MIL-88, a three-dimensional (3D) Fe-based MOF, which was functionalized with boronic acid, affording an efficient immobilization matrix for GLU oxidase [22]. The non-enzymatic sensors exploit MOFs' electrocatalytic ability for the electrooxidation of the GLU by mimicking the enzyme functionality, leading to self-supported electrodes for GLU detection with low detection limits and high sensitivities [21,23–26]. The most reported MOF-modified electrodes concern MOFs that are based on Cu and Ni and lesser on Co and Fe. MOF-14, a 3D porous Cu-MOF, was utilized as a non-enzymatic sensor for the electrochemical determination of GLU, by Zhang and his research team, exhibiting significant stability in alkaline solution and high electrocatalytic activity towards GLU oxidation [23]. Xuan et al. developed a non-enzymatic sweat GLU sensor utilizing a Ni-based MOF, achieving a low detection limit in sweat samples [21]. Fe-based MOFs have also been reported as modifiers in non-enzymatic electrochemical GLU sensors, however, only in blood or serum samples. MIL-53(Fe), an iron-based rod-MOF, was found to enhance the chemiluminescence (CL) of luminol in the presence of H_2O_2 in an alkaline medium [19]. The combination with the GLU oxidase led to an economical, sensitive, and selective CL method for GLU sensing. Furthermore, Fe-MIL-88-NH₂, a MOF based on a trinuclear iron cluster, demonstrates peroxidase-like activity and exhibits high catalytic efficiency and stability as a colorimetric detector for GLU [26] in serum samples.

Our research group focuses on the synthesis of new MOFs based on oxalamide ligands and utilizing them for different purposes such as heavy metal ion sorption, magnetism, and more recently as modifiers in electrochemical sensors [14,27–34]. Herein we report the synthesis, crystal structures, and characterization of a two-dimensional (2D) and a 3D Fe(II)-MOFs which are based on a previously reported oxalamide ligand, H₆L [27]. The two Fe(II)-MOFs were studied towards GLU sorption in aqueous solutions, as well as in artificial sweat solutions. In addition, the 3D-Fe-MOF was also tested as a modifier in a graphite paste electrode (GPE) for the detection of GLU. Preliminary results from the electrochemical application of the modified GPE are discussed.

2. Materials and Methods

2.1. Synthesis and Characterization

All procedures were performed under aerobic conditions. Solvents and reagents were obtained from commercial sources and used as received. The ligand, N,N'-bis(2,4-dicarboxyphenyl)-oxalamide (H₆L), was synthesized following our previously reported method [27]. IR spectra (Figures S1 and S2) were recorded on a Shimadzu FT/IR IRAffinity-1 spectrometer with samples prepared as KBr pellets. Powder X-ray diffraction (pxrd) patterns (Figures S3–S7) were collected on freshly prepared samples on a Bruker D8 Advance X-ray diffractometer (CuK α radiation, $\lambda = 1.5418 \text{ \AA}$). TGA diagrams (Figures S8 and S9) were recorded on a Mettler-Toledo TGA/DSC1 instrument under a N₂ flow of 50 mL/min.

Single Crystal Synthesis of [Fe₂(H₂L)(H₂O)₅], (3D-Fe-MOF)

Here, 0.06 mmol (24 mg) of Fe(NO₃)₃·9H₂O was dissolved in 9 mL H₂O. The yellow clear solution was added to an autoclave containing an N-methyl-2-pyrrolidone (NMP) solution (3 mL) of H₆L 0.06 mmol (25 mg) and 0.24 mmol of LiOH. The autoclave of the yellow blur solution was sealed and placed in an oven at 140 °C. After 2 days yellow needles were formed and collected. FT-IR (KBr disks): 3505 (s), 3419 (s), 3193 (m), 2962 (m), 1703 (m), 1686 (m), 1668 (m), 1653 (m), 1559 (s), 1508 (s), 1451 (s), 1412 (s), 1371 (s), 1301 (m), 1224 (m), 1177 (m), 1080 (w), 961 (w), 922 (w), 908 (w), 895 (w), 866 (w), 813 (m), 777 (m), 692 (w), 557 (m), 527 (m), 497 (m), 419 (m), 402 (w).

Scale-up Synthesis of the 3D-Fe-MOF

Then, 0.8 mmol (323 mg) of $\text{Fe}(\text{NO}_3)_3 \cdot 9\text{H}_2\text{O}$ was dissolved in 24 mL H_2O . The yellow clear solution was added to an autoclave containing an NMP solution (8 mL) of H_6L 0.4 mmol (194 mg) and 1.6 mmol of LiOH. The autoclave of the yellow blur solution was sealed and placed in an oven at 140 °C for 3 days to afford yellow needles. The needles were collected by vacuum filtration, washed extensively with H_2O (5×50 mL), and dried in air. Yield was 82%.

Single Crystal Synthesis of $[\text{Fe}(\text{H}_4\text{L})(\text{H}_2\text{O})_2] \cdot 2\text{H}_2\text{O}$, (2D-Fe-MOF)

In the next step, 0.06 mmol (24 mg) of $\text{Fe}(\text{NO}_3)_3 \cdot 9\text{H}_2\text{O}$ was dissolved in 9 mL H_2O . The yellow clear solution was added to an autoclave containing an NMP solution (3 mL) of H_6L 0.06 mmol (25 mg) and 0.24 mmol of Et_3N . The autoclave with the yellow blur solution was sealed and placed in an oven at 140 °C. After 2 days yellow needles were formed and collected. FT-IR (KBr disks): 3459 (s), 3119 (m), 2930 (m), 2798 (m), 2637 (m), 2538 (m), 2377 (m), 1714 (s), 1677 (m), 1619 (m), 1579 (s), 1508 (s), 1458 (s), 1420 (s), 1384 (s), 1294 (s), 1264 (m), -, 1222 (m), 1172 (m), 1129 (m), 1080 (m), 947 (m), 913 (m), 868 (m), 841 (m), 802 (m), 765 (m), 698 (m), 565 (m), 533 (m), 500 (m), 421 (w), 405 (w), 399 (w).

Scale-up Synthesis of the 2D-Fe-MOF

Finally, 0.2 mmol (81 mg) of $\text{Fe}(\text{NO}_3)_3 \cdot 9\text{H}_2\text{O}$ was dissolved in 27 mL H_2O . The yellow clear solution was added to an autoclave containing an NMP solution (8 mL) of H_6L 0.2 mmol (98 mg) and 0.4 mmol of LiOH. The autoclave of the yellow blur solution was sealed and placed in an oven at 120 °C for 3 days to afford yellow needles. The needles were collected by vacuum filtration, washed extensively with H_2O (5×50 mL), and dried in air. Yield was 65%.

2.2. Single Crystal X-ray Crystallography

The data for the single crystals of the two complexes were collected on a Bruker D8 VENTURE diffractometer (University of Crete), equipped with a PHOTON II CPAD detector, utilizing $\text{Cu-K}\alpha$ ($\lambda = 1.54178 \text{ \AA}$) radiation from an $\text{I}\mu\text{S}$ micro-focus source. Suitable crystals were mounted on a Hampton cryoloop with Paratone-N oil and transferred to a goniostat for data collection. Data integration and reduction were performed using SaintPlus 7.68 A implemented in APEX3 [35]. Absorption correction was performed by the multi-scan method implemented in SADABS [36]. Space groups were determined using XPREP implemented in APEX3 [31]. The structures were solved by direct methods using SHELXT and refined by full-matrix least-squares techniques on F2 with SHELXL contained in the OLEX program package [37,38]. The non-H atoms were treated anisotropically, whereas most H atoms, except some that were found from the Fourier map, were placed in calculated, ideal positions and refined as riding on their respective atoms. Selected crystal data and parameters for data collection are reported in Table S1.

2.3. Sorption Studies

Experimental details concerning the preparation of the standards and the instrumental analysis, including selected reaction monitoring (SRM) transitions of GLU and $\text{GLU-}^{13}\text{C}$ (Table S2) and representative chromatograms of the samples (Figures S10–S12) are given in the supplementary materials.

A GLU solution (6 mM) was prepared by dissolving 0.2706 g of GLU in 250 mL ultra-pure H_2O and its pH value was adjusted to 4.0 with the appropriate addition of hydrochloric acid 0.01 M. The GLU solution was left for 48 h at 4 °C in order to complete its isomerization process. The same procedure was repeated for the artificial sweat sample. The artificial sweat contained 22 mmol L^{-1} urea, 5.5 mmol L^{-1} lactic acid, 3 mmol L^{-1} NH_4Cl , 0.4 mmol L^{-1} CaCl_2 , 50 $\mu\text{mol L}^{-1}$ MgCl_2 , 8 mmol L^{-1} KCl, and 80 mmol L^{-1} NaCl and 25 $\mu\text{mol L}^{-1}$ uric acid (UA). In the above solution, we added 400 $\mu\text{mol L}^{-1}$ GLU. Then, 20 mg of each Fe-MOF absorbent was weighed, and the addition of GLU's solution (10 mL) was followed. The containers were sealed, and the solutions were stirred for four hours. The supernatants were received and centrifuged for 10 min at 3000 rpm. The supernatant solutions were filtered using a cotton filter and the filtrates were transferred to

glass containers where they were stored in the refrigerator (4 °C). The samples were filtered using regenerated cellulose (RC) syringe filters. Appropriate dilutions of the samples (GLU solutions and solutions of artificial sweat) were made with an ACN:H₂O, (80:20, *v/v*) solvent mixture (ACN = acetonitrile) so that their concentrations were within the linear range of the GLU standards used for their quantification. The internal standard (IS) was used to correct for possible instrumental instability.

Six working solutions with various concentrations ranging from 0.5–40 mg L⁻¹ were prepared via appropriate dilution of a GLU solution (100 mg L⁻¹) in ACN:H₂O, (80:20, *v/v*), while GLU-¹³C (IS) was added to each solution at the same concentration (10 mg L⁻¹). The ratio of the peak area of GLU to the peak area of the IS was used for the construction of the calibration curve. Additionally, the matrix effect has been investigated through the preparation of matrix-matched samples at the concentration of 10 mg L⁻¹.

The final concentrations of the GLU solutions were determined with UPLCMS/MS. Finally, the sorption capacity (*S* in mg_{GLU}/g_{MOF}) was determined by the following equation:

$$S = \frac{(C_i - C_f) \cdot V}{m_{\text{MOF}}} \quad (1)$$

where *V* is the volume of GLU solution (0.010 L) where the material was dispersed and *m*_{MOF} is the weight of the material (0.020 g).

2.4. Electrochemical Application

A stock solution of 0.1 M GLU was prepared in water and stored at 4 °C until use. Phosphate buffer 0.10 M, pH 6.0 was prepared by dissolving the appropriate amounts of Na₂HPO₄·2H₂O (Chem Lab) and NaH₂PO₄·2H₂O (Chem Lab) in water, and the pH value was adjusted using 1 M HCl solution. For the preparation of all solutions, Milli-Q-grade water was used.

Fabrication of the modified graphite paste electrode

Modified graphite paste electrode (GPE) was fabricated by mixing 0.95 g graphite powder (grade #38, Fisher Scientific, Pittsburgh, PA, USA), 0.05 g of 3D-Fe-MOF and 0.4 g paraffin (Merck, Rahway, NJ, USA). The resulting paste was filled up in a plastic syringe and a copper wire passing through the paste was used to achieve electric contact. The surface of the modified GPE was flattened by pressing the edge of the syringe on tissue paper, while the electrode surface was renewed via a slight pressure on the syringe plunger and polishing it on filter paper for further use.

Voltammetric measurements

All electrochemical measurements were carried out with a portable EmStat3 potentiostat (Palm Sens, Houten, The Netherlands) combined with the PS Trace 4.2 software (Palm Sens). A three-electrodes system was used with the modified GPE acting as the working electrode, a saturated calomel electrode (SCE) as a reference electrode and a Pt wire as the counter electrode. Differential pulse (DP) voltammetric measurements were carried out under the following conditions: the potential range was from -1.40 to 1.9 V, the modulation amplitude was 0.05 V, the modulation time was 0.02 s, the step potential was 2 mV, and the scan rate was 20 mV/s. All measurements were performed in a voltammetric cell containing 25.0 mL of the working solution. The peak currents of voltammograms were used for the quantitative detection of GLU.

3. Results and Discussion

3.1. Synthesis

As mentioned above [14,27–34], we investigated oxalamide ligands for the synthesis of new MOFs. Given that N,N'-bis(2,4-dicarboxyphenyl)-oxalamide (H₆L) has already been reported to react with alkaline earths, lanthanides, and 3d transition metal, we extended our studies with iron salts from, which we obtained the two new iron-based MOFs after conducting a large amount of solvothermal experiments. The solvents that were tested were dimethylformamide (DMF), dimethylacetamide (DMA), N-methyl-2-pyrrolidone (NMP),

water (H₂O), methanol (MeOH) and ethanol (EtOH) and mixtures of them. To this end, we found that both iron-MOFs were best prepared by a 3:1 mixture of H₂O and NMP in the presence of a base.

For the deprotonation of the ligands, we tested both inorganic and organic bases, such as LiOH, NaOH, KOH, Et₄NOH, and Et₃N. In the case of the 3D-Fe-MOF, four equivalents of LiOH led to the tetra-anion of the ligand (H₂L⁴⁻) while the ligand in the 2D-Fe-MOF is only twice deprotonated (H₄L²⁻). It is worth noting that four equivalents of the weak base Et₃N were not enough to deprotonate the oxalamide ligand four times. The degree of deprotonation of the ligand is crucial for the formation of the final product since the H₄L²⁻ led to the 2D-Fe-MOF, while the H₂L⁴⁻ to the 3D-Fe-MOF. Besides the kind and amount of base used, concentration, as well as the temperature, affect the final product, as discovered during the scale-up experiments. For the scale-up synthesis of the 3D-Fe-MOF, only the adjustment of the equivalents of iron nitrate to H₆L to 2:1 (and four equivalents of LiOH) was needed to succeed with an 82% yield. However, when we tried to scale up the synthesis of the 2D-Fe-MOF the increased concentration, the four equivalents of Et₃N, and the temperature of 140 °C led to the 3D-Fe-MOF instead. To this end, after several attempts, we managed to scale up the synthesis of the 2D-Fe-MOF with the use of two equivalents of LiOH at a temperature of 120 °C which led to pure 2D-Fe-MOF, with a yield of 65%.

Although it has been stated that the influence of metal-ligand ratios on the structure of the resulting compounds is important [39], in this case, the degree of deprotonation of the ligand has a stronger effect than the metal-ligand ratio.

The reduction of the trivalent iron that was used in the first place is also noteworthy. Trivalent iron nitrate was selected for the first experiments because of its good solubility in water and its low price. However, in both products, Fe(III) was reduced to Fe(II) as confirmed by the bond-valence sum (BVS) calculations (Table S3). This kind of iron reduction has already been reported in the literature several times and it is possibly attributed to the usage of NMP at high temperatures [40–43]. We also tried to obtain the products by reacting H₆L with divalent iron salts such as FeCl₂·4H₂O and Fe(ClO₄)₂·6H₂O. Although both salts afforded the two MOFs, yields were considerably reduced (i.e., 5–10%) and the scale-up experiments showed colored impurities, especially, in the case of the FeCl₂·4H₂O. Therefore, the best results were obtained by the use of the trivalent iron salt, Fe(NO₃)₃·9H₂O, with the pXRD analysis (Figures S5 and S6) revealing high purity and water stability (the products were extensively washed with H₂O during filtration) for each product.

3.2. Description of Structures

3D-Fe-MOF crystallizes in the triclinic space group *P*-1. The asymmetric unit comprises two crystallographically independent Fe(II) ions, a tetra-anion of the organic ligand (H₂L⁴⁻), and 5 coordinated water molecules (Figure S13). Both metal centers adopt a slightly distorted octahedral geometry. The Fe1 is surrounded by four carboxylate O atoms and two O atoms from two terminal H₂O (Figure S14). The coordination sphere of Fe2 contains three carboxylate O atoms and three terminal H₂O (Figure S14). The H₂L⁴⁻ ligand adopts a *trans* conformation bridging seven different iron ions (Figure S15). There are three kinds of carboxylates. Two of the four carboxylates (C1, C13) of the ligand act as μ₂-η¹:η¹ bridges leading to the formation of two alternating Fe1–Fe2 rods down the crystallographic axis *a*. The third carboxylate C18 acts, also, as a μ₂-η¹:η¹ bridge between Fe1 and Fe2 belonging to two different rods leading to a double rod ladder. The final carboxylate C8 acts as a terminal monodentate O donor. In this arrangement, a 3D framework is formed (Figure 1). For the topological analysis of the framework, we utilized six different nodes. Three of the four carboxylate carbon atoms C1, C13, and C18 serve as 5-coordinated nodes while C8 serves as a 3-coordinated node. Finally, the two centroids of the benzene rings of the ligand serve as two 3-coordinated nodes with the ligand serving as two fused 3-coordinated nodes. This leads to a new 3,3,3,5,5,5-c network (Figure 2) with the following point symbol {3.4².5.6².7.8³}{3.4².5.6³.7².8}{3.4³.5².6².7.8}{4.6.8}{6.8²}.₂.

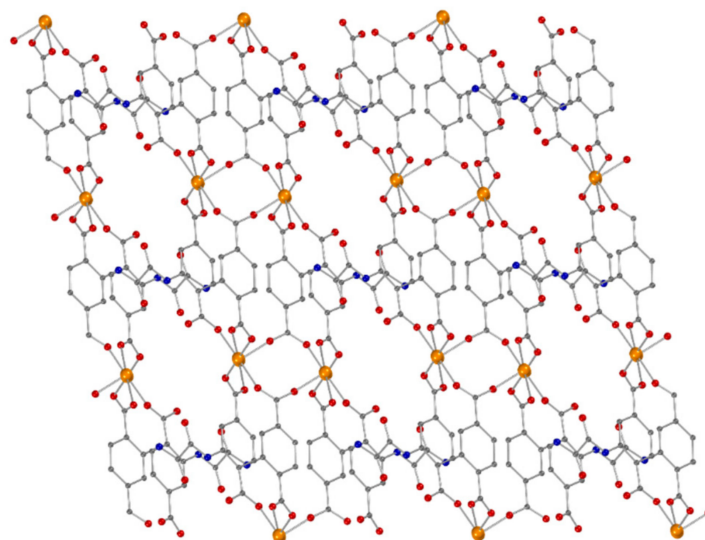


Figure 1. The 3D framework of the 3D-Fe-MOF down to the a axis. Color code: Fe orange, C, grey, H cyan, O red, N blue.

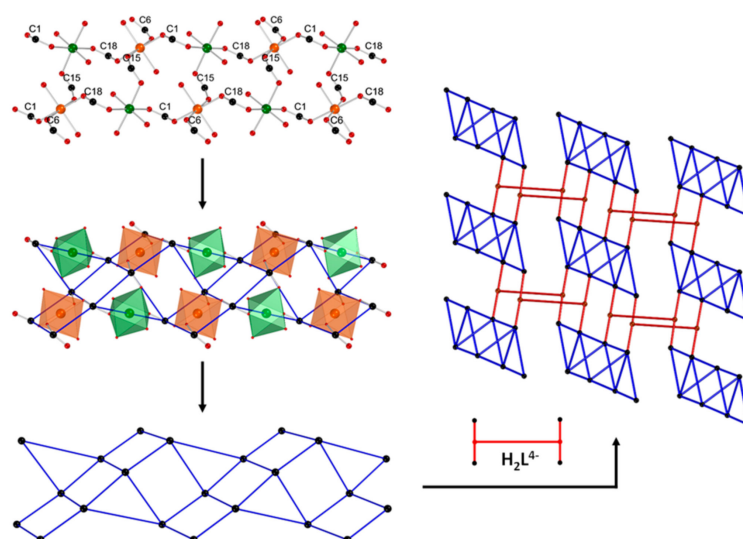


Figure 2. The deconstruction of the 3D framework of the 3D-Fe-MOF. Color code: Fe1 green, Fe2 orange, C black, O red, H_2L^{4-} dark red lines.

2D-Fe-MOF crystallizes in the monoclinic space group $P2_1n$. The asymmetric unit contains half Fe(II) ion, half organic ligand (H_4L^{2-}) two times deprotonated, and two water molecules, one coordinated and one in the lattice (Figure S16). The metal center adopts a slightly distorted octahedral geometry, where the equatorial oxygens are originated from four carboxylates from four different ligands and the two axial oxygens from the two water molecules (Figure S17). The H_4L^{2-} ligand bridges two different iron ions adopting *trans* conformation (Figure S17) leading to a two-dimensional network (Figure 3). The deprotonated carboxylates act as μ_2 - η^1 : η^1 bridges forming an iron rod down the crystallographic axis b . In addition, hydrogen bonds can be observed in the structure. There are four different types of hydrogen bonds with the water molecule in the lattice that bind the two-dimensional layers extending the network to the third dimension. From the topological point of view, each deprotonated carboxylate serves as a four-coordinated node forming an **sql** network with a point symbol $(4^4.6^2)$ (Figure S18).

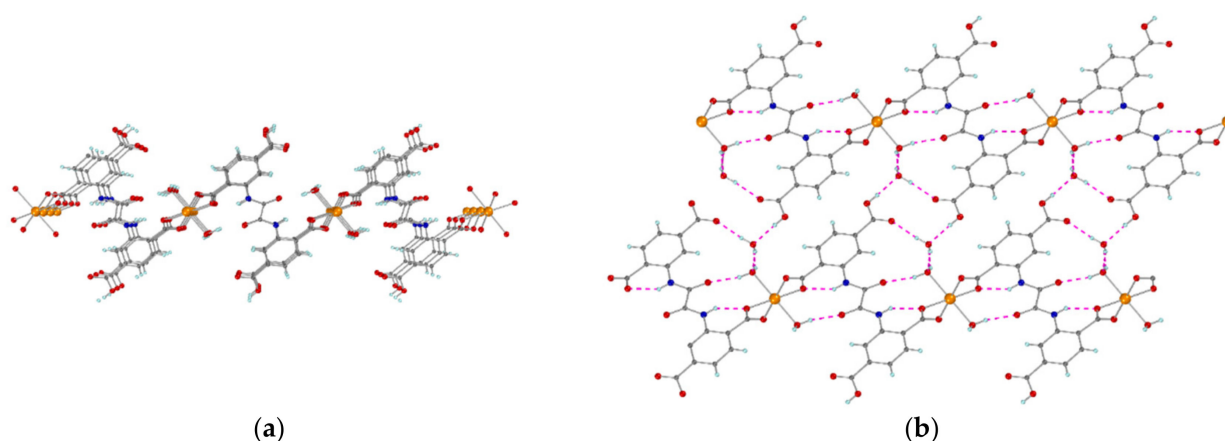


Figure 3. Two views of the 2D framework of **2D-Fe-MOF**. (a) A single layer down to the *b* axis and (b) two neighboring layers down to *b* axis showing the intra- and inter-layer hydrogen bonding (purple dashed lines). Color code: Fe orange, C, grey, H cyan, O red, N blue.

3.3. Sorption Study

Although neither of the two MOFs has an open (porous) framework, we tried to study both materials for GLU sorption, given their water stability. To the best of our knowledge, GLU sorption by MOFs has never been reported before even when electrochemical research is included. Herein, we investigated the sorption ability of both Fe-MOFs of GLU's solution at pH 4.0 as well as the sorption ability of artificial sweat at the same pH value.

The capacity of **3D-Fe-MOF** sorption for the GLU solution and artificial sweat was 15 mg/g and 1.0 mg/g, respectively, whereas for **2D-Fe-MOF** were 3.4 mg/g and 2.5 mg/g.

The quantitative results were derived from the standard calibration curve corrected with IS. The correlation coefficient of the standards calibration curve corrected with the IS being 0.9998, whereas the intercept did not differ significantly from zero, as presented in Equation (2). The instrumental Limit of Detection was 0.15 mg/L, which was calculated as the concentration at which the signal-to-noise ratio was above 3.3.

$$y = (0.0489 \pm 0.0035)x + (-0.017 \pm 0.086) \quad (2)$$

Additionally, neither suppression nor enhancement of the analytical signal was observed based on the obtained recoveries. As expected, the observed GLU sorption of both MOFs is negligible and whatever sorption is observed can only be described as superficial.

3.4. Preliminary Electrochemical Evaluation of the GPE Modified with 3D-Fe-MOF

The modified graphite paste electrode was tested for the enzyme-free detection of GLU. Figure 4 presents the DP voltammograms of the modified GPEs loaded with 1%, 2%, or 5% (*w/w*) **3D-Fe-MOF** for the detection of 0.6 mM GLU in phosphate buffer 0.10 M, pH 6.0. Among the three synthesized GPEs, the 5% (*w/w*) exhibited a higher voltammetric response for GLU.

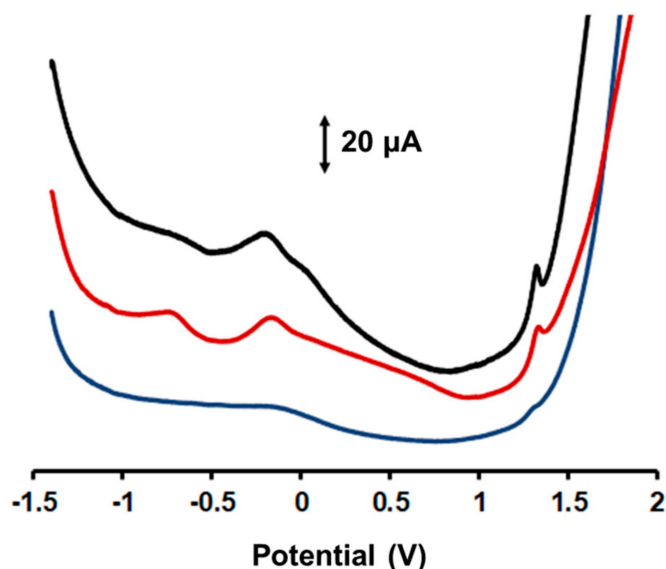
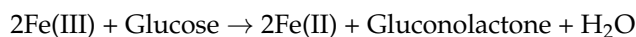


Figure 4. DP voltammograms of 0.6 mM GLU in 0.10 M phosphate buffer, pH 6.0 at the modified GPEs loaded with 1% (black line), 2% (red line), and 5% (blue line) *w/w* 3D-Fe-MOF.

Figure 5 presents the background-subtracted DP voltammograms at the modified GPE with the 3D-Fe-MOF for the detection of three different concentrations of GLU between 100–300 μM in phosphate buffer 0.10 M (pH 6.0). The limit of detection (LOD) was conditionally calculated as 22 μM but work is in progress to further decrease this value. The performance of the GPE modified with the 3D-Fe-MOF was tested in artificial sweat (pH 4.0) containing 500 μM GLU and a well-defined voltammetric peak was obtained (Figure S19) indicating the potential scope of this sensor for GLU detection in sweat.

A possible mechanism for GLU detection is [44,45]:



Derived from 3D-Fe-MOF, Fe(III) is in situ formed during the voltammetric scan initiated from -1.4 V.

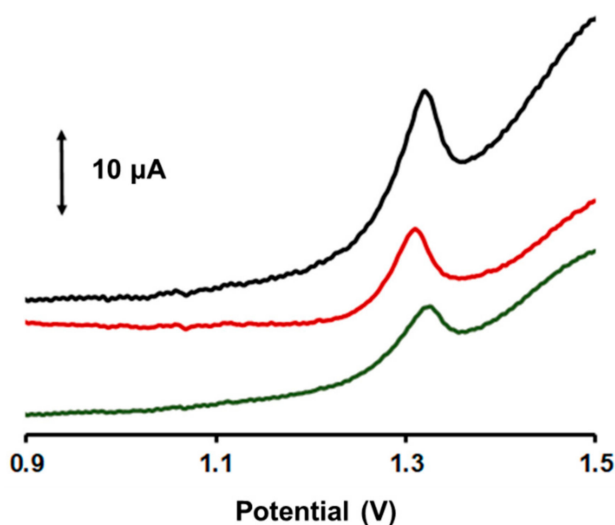


Figure 5. Background-subtracted DP voltammograms for GLU concentrations in the range of 100–300 μM in phosphate buffer 0.1 M, pH 6 obtained with the modified GPE.

4. Conclusions

Two new Fe(II) MOFs based on the oxalamide ligand *N,N'*-bis(2,4-dicarboxyphenyl)-oxalamide (H_6L) have been synthesized and structurally characterized by single crystal and powder X-ray diffraction methods. Depending on the reaction conditions and the degree of the deprotonation of the bridging ligand, a 2D and a 3D Fe(II)-MOF were isolated. Both MOFs were found to maintain their structure in an aqueous solution as evidenced by pXRD data. The investigation of the sorption ability of GLU from aqueous solutions by both Fe-MOFs indicated very little or negligible sorption. We fabricated a graphite paste electrode using the **3D-Fe-MOF** as a modifier for the non-enzymatic GLU detection in an aqueous solution at pH 6. Preliminary results indicated that the **3D-Fe-MOF**-modified GPE is capable of detecting GLU. Work is in progress for the optimization and development of a **3D-Fe-MOF**-modified electrode for the quantitative determination of GLU in aqueous solutions.

Supplementary Materials: The following supporting information can be downloaded at: <https://www.mdpi.com/article/10.3390/chemistry5010002/s1>, Table S1: Crystal data and structure refinement for the two compounds; Table S2: Selected reaction monitoring (SRM) transitions of GLU and GLU- ^{13}C ; Table S3: Bond Valence Sums (BVS) for the iron atoms in the two structures. (R_o and B values for each calculation. Fe^{II} : $R_o = 1.734$, $B = 0.37$, Fe^{III} : $R_o = 1.759$, $B = 0.37$); Figure S1: The IR spectra (KBr disc) of $[Fe_2(H_2L)(H_2O)_5]$. Free N-H vibration is observed at around 3505 cm^{-1} . C-N stretching vibration is found at 1301 cm^{-1} . The stretching vibrations $\nu(C=O)$ of the carbonyl group is observed at 1668 cm^{-1} . The peaks 1559 cm^{-1} and 1451 cm^{-1} are attributed to the asymmetric vibrations of the deprotonated carboxylates while at 1508 cm^{-1} and 1412 cm^{-1} to the respective symmetric vibrations. The stretch of the C=O of the carboxylate which is anticipated at around 1710 cm^{-1} is absent due to the tetra-deprotonation of the ligand; Figure S2: The IR spectra (KBr disc) of $[Fe(H_4L)(H_2O)_2]\cdot 2H_2O$. Free N-H absorption is observed at around 3459 cm^{-1} . C-N stretching vibration is found at 1294 cm^{-1} . The stretching vibrations $\nu(C=O)$ of the carbonyl group is observed at 1677 cm^{-1} . The peaks 1579 cm^{-1} and 1458 cm^{-1} are attributed to the asymmetric vibrations of the deprotonated carboxylates while at 1508 cm^{-1} and 1420 cm^{-1} to the respective symmetric vibrations. Because of the deprotonation of the ligand (H_4L^{-2}), the stretch of the C=O of the carboxylate can be observed at 1714 cm^{-1} ; Figure S3: The PXR patterns of $[Fe_2(H_2L)(H_2O)_5]$; Figure S4: Le Bail refinement plot showing the experimental, simulated (reverted) and difference powder diffraction patterns of $[Fe_2(H_2L)(H_2O)_5]$. Vertical markers refer to the calculated positions of the Bragg reflections. $R_p = 4.281$, $R_{wp} = 7.104$, Weighting scheme: $w = 1.0/y_{count}$, Profile function: Pearson VII; Figure S5: The PXR patterns of $[Fe(H_4L)(H_2O)_2]\cdot 2H_2O$; Figure S6: Le Bail refinement plot showing the experimental, simulated (reverted) and difference powder diffraction patterns of $[Fe(H_4L)(H_2O)_2]\cdot 2H_2O$. Vertical markers refer to the calculated positions of the Bragg reflections. $R_p = 6.038$, $R_{wp} = 7.153$, Weighting scheme: $w = 1.0/y_{count}^2$, Profile function: Pseudo-Voigt; Figure S7: The PXR patterns of the graphite paste (red line), of the $[Fe_2(H_2L)(H_2O)_5]$ (black line) and of the graphite paste with 5% of $[Fe_2(H_2L)(H_2O)_5]$ (blue line). Besides the low percentage of the MOF and the preferred orientation of the pattern, characteristic peaks of the MOF are visible in the pXRD of the enriched graphite paste; Figure S8: Thermogravimetric analysis reveals that $[Fe_2(H_2L)(H_2O)_5]$ losses $\sim 13.69\%$ within $25\text{--}260\text{ }^\circ\text{C}$ temperature range which is very close to the theoretical value of the five coordinated H_2O molecules (theoretical value 14.65%). The residue above $360\text{ }^\circ\text{C}$ is $\sim 27.65\%$ which corresponds to Fe_2O_3 (theoretical value 26.05%); Figure S9: The Thermographic analysis of $[Fe(H_4L)(H_2O)_2]\cdot 2H_2O$. Thermogravimetric analysis reveals that $[Fe(H_4L)(H_2O)_2]\cdot 2H_2O$ losses $\sim 6.45\%$ within $25\text{--}170\text{ }^\circ\text{C}$ temperature range which is very close to the theoretical value of the two H_2O molecules in the lattice (theoretical value 6.64%) followed by a loss of $\sim 6.96\%$ within the $170\text{--}260\text{ }^\circ\text{C}$ that can be attributed to the loss of the two coordinated H_2O molecules (theoretical value 6.64%). The residue above $360\text{ }^\circ\text{C}$ is $\sim 17.83\%$ which corresponds to Fe_2O_3 (theoretical value 20.06%); Figure S10: Representative chromatogram of (a) GLU solution (20 mg L^{-1}) used for the absorption (b) the supernatant solution of GLU, using as absorbent the **3D-Fe-MOF** (where GLU (Q) is the quantifier ion of GLU, GLU (q) is the qualifier ion of GLU, and GLU- ^{13}C (IS) is the most abundant ion for the internal standard (IS); Figure S11: Representative chromatogram of (a) GLU standard solution (20 mg L^{-1}) (b) GLU solution used for the absorption (20 mg L^{-1}) (c) the supernatant solution of artificial sweat using as absorbent the **3D-Fe-MOF** (where GLU (Q) is the quantifier ion of GLU, GLU (q) is the qualifier ion of GLU, and GLU- ^{13}C (IS) is the most abundant ion for the internal standard GLU- ^{13}C (IS);

Figure S12: Representative chromatogram of (a) standard GLU solution (20 mg L⁻¹) (b) supernatant solution of artificial sweat using as absorbent the 2D-Fe-MOF (where GLU (Q) is the quantifier ion of GLU, GLU (q) is the qualifier ion of GLU, and GLU-¹³C (IS) is the most abundant ion for the internal standard GLU-¹³C; Figure S13: The asymmetric unit of the 3D-Fe-MOF. Color code: Fe orange, C, grey, H cyan, O red, N blue; Figure S14: The coordination environment around Fe1 (left) and Fe2 (right) in the crystal structure of the 3D-Fe-MOF. Color code: same as in Figure S13; Figure S15: The coordination mode of the tetra-anion of the ligand (H₂L⁴⁻) in the crystal structure of the 3D-Fe-MOF. Color code: same as in Figure S13; Figure S16: The asymmetric unit of the 2D-Fe-MOF. Color code: Fe orange, C, grey, H cyan, O red, N blue; Figure S17: The coordination environment around Fe (left) and the coordination mode of the di-anion of the ligand (H₄L²⁻) (right) in the crystal structure of the 2D-Fe-MOF. Color code: same as in Figure S16; Figure S18: The underline sq1 network of the 2D-Fe-MOF. Color code: same as in Figure S13; Figure S19: DP voltammograms of 0 and 600 μM GLU at the GPE modified with the 3D-Fe-MOF in artificial sweat (pH 4.0).

Author Contributions: Conceptualization, G.S.P. and C.K.; investigation, P.O., V.P., E.K., A.P., M.G.K. and T.G.T.; resources, G.S.P., C.K., A.E. and N.S.T.; writing—original draft preparation, G.S.P.; writing—review and editing, G.S.P.; visualization, G.S.P.; supervision, G.S.P., N.S.T. and C.K. All authors have read and agreed to the published version of the manuscript.

Funding: This research has been co-financed by the European Regional Development Fund of the European Union and Greek national funds through the Operational Program Competitiveness, Entrepreneurship and Innovation, under the call RESEARCH—CREATE—INNOVATE (project code: T2EDK-00028/MIS 5067540).

Institutional Review Board Statement: Not applicable.

Informed Consent Statement: Not applicable.

Data Availability Statement: Not applicable.

Conflicts of Interest: The authors declare no conflict of interest. The funders had no role in the design of the study; in the collection, analyses, or interpretation of data; in the writing of the manuscript; or in the decision to publish the results.

References

1. Galant, A.L.; Kaufman, R.C.; Wilson, J.D. GLU: Detection and Analysis. *Food Chem.* **2015**, *188*, 149–160. [[CrossRef](#)] [[PubMed](#)]
2. Sehit, E.; Altintas, Z. Significance of Nanomaterials in Electrochemical GLU Sensors: An Updated Review (2016–2020). *Biosens. Bioelectron.* **2020**, *159*, 112165. [[CrossRef](#)] [[PubMed](#)]
3. Heller, A.; Feldman, B. Electrochemistry in Diabetes Management. *Acc. Chem. Res.* **2010**, *43*, 963–973. [[CrossRef](#)] [[PubMed](#)]
4. Guth, U.; Vonau, W.; Zosel, J. Recent Developments in Electrochemical Sensor Application and Technology—A Review. *Meas. Sci. Technol.* **2009**, *20*, 14. [[CrossRef](#)]
5. Bandodkar, A.J.; Jeang, W.J.; Ghaffari, R.; Rogers, J.A. Wearable Sensors for Biochemical Sweat Analysis. *Annu. Rev. Anal. Chem.* **2019**, *12*, 201–224. [[CrossRef](#)]
6. Karpova, E.V.; Karyakina, E.E.; Karyakin, A.A. Wearable Non-Invasive Monitors of Diabetes and Hypoxia through Continuous Analysis of Sweat. *Talanta* **2020**, *215*, 120922. [[CrossRef](#)]
7. Xue, Q.; Li, Z.; Wang, Q.; Pan, W.; Chang, Y.; Duan, X. Nanostrip Flexible Microwave Enzymatic Biosensor for Noninvasive Epidermal GLU Sensing. *Nanoscale Horiz.* **2020**, *5*, 934–943. [[CrossRef](#)]
8. Park, S.; Boo, H.; Chung, T.D. Electrochemical Non-Enzymatic GLU Sensors. *Anal. Chim. Acta* **2006**, *556*, 46–57. [[CrossRef](#)]
9. Hwang, D.W.; Lee, S.; Seo, M.; Chung, T.D. Recent Advances in Electrochemical Non-Enzymatic GLU Sensors—A Review. *Anal. Chim. Acta* **2018**, *1033*, 1–34. [[CrossRef](#)]
10. Katseli, V.; Economou, A.; Kokkinos, C. Smartphone-Addressable 3D-Printed Electrochemical Ring for Nonenzymatic Self-Monitoring of GLU in Human Sweat. *Anal. Chem.* **2021**, *93*, 3331–3336. [[CrossRef](#)]
11. Abrori, S.A.; Septiani, N.L.W.; Nugraha; Anshori, I.; Suyatman; Suendo, V.; Yulianto, B. Metal-Organic-Framework Fe₃O₄-Derived Fe₃O₄ for Non-Enzymatic Electrochemical Detection of GLU. *Sensors* **2020**, *20*, 4891. [[CrossRef](#)]
12. Vasiliou, F.; Plessas, A.K.; Economou, A.; Thomaidis, N.; Papaefstathiou, G.S.; Kokkinos, C. Graphite Paste Sensor Modified with a Cu(II)-Complex for the Enzyme-Free Simultaneous Voltammetric Determination of GLU and Uric Acid in Sweat. *J. Electroanal. Chem.* **2022**, *917*, 116393. [[CrossRef](#)]
13. Zhou, H.C.; Long, J.R.; Yaghi, O.M. Introduction to Metal-Organic Frameworks. *Chem. Rev.* **2012**, *112*, 673–674. [[CrossRef](#)] [[PubMed](#)]
14. Moutzouris, N.; Moushi, E.E.; Tziotzi, T.G.; Tarlas, G.D.; Tasiopoulos, A.J.; Escuer, A.; Papaefstathiou, G.S. Metallo-Ligand Based 3d/4f Coordination Polymers: Synthesis, Structure and Magnetic Properties. *Eur. J. Inorg. Chem.* **2022**, *12*, e202200024. [[CrossRef](#)]

15. Li, L.; Zou, J.; Han, Y.; Liao, Z.; Lu, P.; Nezamzadeh-Ejehieh, A.; Liu, J.; Peng, Y. Recent advances in Al(iii)/In(iii)-based MOFs for the detection of pollutants. *N. J. Chem.* **2022**, *46*, 19577–19592. [[CrossRef](#)]
16. Zheng, M.; Chen, J.; Zhang, L.; Cheng, Y.; Lu, C.; Liu, Y.; Singh, A.; Trivedi, M.; Kumar, A.; Liu, J. Metal Organic Frameworks as Efficient Adsorbents for Drugs from Wastewater. *Mater. Today Commun.* **2022**, *31*, 103514. [[CrossRef](#)]
17. Zhong, Y.; Chen, C.; Liu, S.; Lu, C.; Liu, D.; Pan, Y.; Sakiyama, H.; Muddassir, M.; Liu, J. A New Magnetic Adsorbent of Eggshell-Zeolitic Imidazolate Framework for Highly Efficient Removal of Norfloxacin. *Dalton Trans.* **2021**, *50*, 18016–18026. [[CrossRef](#)] [[PubMed](#)]
18. Dong, X.; Li, Y.; Li, D.; Liao, D.; Qin, T.; Prakash, O.; Kumar, A.; Liu, J. A New 3D 8-Connected Cd(II) MOF as a Potent Photocatalyst for Oxytetracycline Antibiotic Degradation. *CrystEngComm* **2022**, *24*, 6933–6943. [[CrossRef](#)]
19. Yi, X.; Dong, W.; Zhang, X.; Xie, J.; Huang, Y. MIL-53(Fe) MOF-Mediated Catalytic Chemiluminescence for Sensitive Detection of GLU. *Anal. Bioanal. Chem.* **2016**, *408*, 8805–8812. [[CrossRef](#)]
20. Hu, Q.; Qin, J.; Wang, X.F.; Ran, G.Y.; Wang, Q.; Liu, G.X.; Ma, J.P.; Ge, J.Y.; Wang, H.Y. Cu-Based Conductive MOF Grown in Situ on Cu Foam as a Highly Selective and Stable Non-Enzymatic GLU Sensor. *Front. Chem.* **2021**, *9*, 786970. [[CrossRef](#)]
21. Xuan, X.; Qian, M.; Pan, L.; Lu, T.; Han, L.; Yu, H.; Wan, L.; Niu, Y.; Gong, S. A Longitudinally Expanded Ni-Based Metal-Organic Framework with Enhanced Double Nickel Cation Catalysis Reaction Channels for a Non-Enzymatic Sweat GLU Biosensor. *J. Mater. Chem. B* **2020**, *8*, 9094–9109. [[CrossRef](#)] [[PubMed](#)]
22. Zhao, Z.; Huang, Y.; Liu, W.; Ye, F.; Zhao, S. Immobilized GLU Oxidase on Boronic Acid-Functionalized Hierarchically Porous MOF as an Integrated Nanozyme for One-Step GLU Detection. *ACS Sustain. Chem. Eng.* **2020**, *8*, 4481–4488. [[CrossRef](#)]
23. Zhang, D.; Zhang, J.; Zhang, R.; Shi, H.; Guo, Y.; Guo, X.; Li, S.; Yuan, B. 3D Porous Metal-Organic Framework as an Efficient Electrocatalyst for Nonenzymatic Sensing Application. *Talanta* **2015**, *144*, 1176–1181. [[CrossRef](#)] [[PubMed](#)]
24. Zhang, L.; Ding, Y.; Li, R.; Ye, C.; Zhao, G.; Wang, Y. Ni-Based Metal-Organic Framework Derived Ni@C Nanosheets on a Ni Foam Substrate as a Supersensitive Non-Enzymatic GLU Sensor. *J. Mater. Chem. B* **2017**, *5*, 5549–5555. [[CrossRef](#)]
25. Zhang, L.; Ma, X.; Liang, H.; Lin, H.; Zhao, G. A Non-Enzymatic GLU Sensor with Enhanced Anti-Interference Ability Based on a MIL-53(NiFe) Metal-Organic Framework. *J. Mater. Chem. B* **2019**, *7*, 7006–7013. [[CrossRef](#)]
26. Liu, Y.L.; Zhao, X.J.; Yang, X.X.; Li, Y.F. A Nanosized Metal-Organic Framework of Fe-MIL-88NH₂ as a Novel Peroxidase Mimic Used for Colorimetric Detection of GLU. *Analyst* **2013**, *138*, 4526–4531. [[CrossRef](#)]
27. Margariti, A.; Rapti, S.; Katsenis, A.D.; Friščić, T.; Georgiou, Y.; Manos, M.J.; Papaefstathiou, G.S. Cu²⁺ Sorption from Aqueous Media by a Recyclable Ca²⁺ Framework. *Inorg. Chem. Front.* **2017**, *4*, 773–781. [[CrossRef](#)]
28. Margariti, A.; Pournara, A.D.; Manos, M.J.; Lazarides, T.; Papaefstathiou, G.S. Towards White-Light Emission by Tb³⁺/Eu³⁺ Substitution in a Ca²⁺ Framework. *Polyhedron* **2018**, *153*, 24–30. [[CrossRef](#)]
29. Tarlas, G.D.; Katsenis, A.D.; Papaefstathiou, G.S. An I2O1 Barium Framework Derived from an In-Situ Metal-Assisted Ligand Transformation. *Eur. J. Inorg. Chem.* **2018**, *2018*, 4458–4464. [[CrossRef](#)]
30. Pournara, A.D.; Tarlas, G.D.; Papaefstathiou, G.S.; Manos, M.J. Chemically Modified Electrodes with MOFs for the Determination of Inorganic and Organic Analytes via Voltammetric Techniques: A Critical Review. *Inorg. Chem. Front.* **2019**, *6*, 3440–3455. [[CrossRef](#)]
31. Pournara, A.D.; Margariti, A.; Tarlas, G.D.; Kourtellaris, A.; Petkov, V.; Kokkinos, C.; Economou, A.; Papaefstathiou, G.S.; Manos, M.J. A Ca²⁺ MOF Combining Highly Efficient Sorption and Capability for Voltammetric Determination of Heavy Metal Ions in Aqueous Media. *J. Mater. Chem. A* **2019**, *7*, 15432–15443. [[CrossRef](#)]
32. Kokkinos, C.; Economou, A.; Pournara, A.; Manos, M.; Spanopoulos, I.; Kanatzidis, M.; Tziotzi, T.; Petkov, V.; Margariti, A.; Oikonomopoulos, P.; et al. 3D-Printed Lab-in-a-Syringe Voltammetric Cell Based on a Working Electrode Modified with a Highly Efficient Ca-MOF Sorbent for the Determination of Hg(II). *Sens. Actuators B Chem.* **2020**, *321*, 128508. [[CrossRef](#)]
33. Margariti, A.; Moushi, E.; Tasiopoulos, A.J.; Escuer, A.; Papaefstathiou, G.S. Oxalamide Based Coordination Polymers. *J. Coord. Chem.* **2021**, *74*, 252–265. [[CrossRef](#)]
34. Vlachou, E.; Margariti, A.; Papaefstathiou, G.S.; Kokkinos, C. Voltammetric Determination of Pb(II) by a Ca-MOF-Modified Carbon Paste Electrode Integrated in a 3D-Printed Device. *Sensors* **2020**, *20*, 4442. [[CrossRef](#)]
35. Bruker. APEX2 (v2010.5-0); Bruker AXS Inc.: Madison, WI, USA, 2010.
36. Sheldrick, G.M. *Program for Empirical Absorption Correction of Area Detector Data*; University of Gottingen: Gottingen, Germany, 1996.
37. Sheldrick, G.M. A Short History of SHELX. *Acta Crystallogr. Sect. A Found. Crystallogr.* **2008**, *64*, 112–122. [[CrossRef](#)]
38. Dolomanov, O.V.; Bourhis, L.J.; Gildea, R.J.; Howard, J.A.K.; Puschmann, H. OLEX2: A Complete Structure Solution, Refinement and Analysis Program. *J. Appl. Crystallogr.* **2009**, *42*, 339–341. [[CrossRef](#)]
39. Zhao, J.P.; De Han, S.; Zhao, R.; Yang, Q.; Chang, Z.; Bu, X.H. Tuning the Structure and Magnetism of Heterometallic Sodium(1+)-Cobalt(2+) Formate Coordination Polymers by Varying the Metal Ratio and Solvents. *Inorg. Chem.* **2013**, *52*, 2862–2869. [[CrossRef](#)]
40. Mylonas-Margaritis, I.; Mayans, J.; Tong, W.; Farràs, P.; Escuer, A.; McArdle, P.; Papatriantafyllopoulou, C. Synthesis and Characterization of New Coordination Compounds by the Use of 2-Pyridinemethanol and Di- or Tricarboxylic Acids. *CrystEngComm* **2021**, *23*, 5489–5497. [[CrossRef](#)]
41. Zhao, J.P.; Xu, J.; De Han, S.; Wang, Q.L.; Bu, X.H. A Niccolite Structural Multiferroic Metal–Organic Framework Possessing Four Different Types of Bistability in Response to Dielectric and Magnetic Modulation. *Adv. Mater.* **2017**, *29*, 1606966. [[CrossRef](#)]
42. Li, Y.W.; Yan, H.; Hu, T.L.; Ma, H.Y.; Li, D.C.; Wang, S.N.; Yao, Q.X.; Dou, J.M.; Xu, J.; Bu, X.H. Two Microporous Fe-Based MOFs with Multiple Active Sites for Selective Gas Adsorption. *Chem. Commun.* **2017**, *53*, 2394–2397. [[CrossRef](#)]

43. Zhang, T.Z.; Lu, Y.; Li, Y.G.; Zhang, Z.; Chen, W.L.; Fu, H.; Wang, E.B. Metal-Organic Frameworks Constructed from Three Kinds of New Fe-Containing Secondary Building Units. *Inorganica Chim. Acta* **2012**, *384*, 219–224. [[CrossRef](#)]
44. Neravathu, D.; Paloly, A.R.; Sajan, P.; Satheesh, M.; Bushiri, M.J. Hybrid nanomaterial of ZnFe₂O₄/α-Fe₂O₃ implanted graphene for electrochemical glucose sensing application. *Diam. Relat. Mater.* **2020**, *106*, 107852. [[CrossRef](#)]
45. Xia, C.; Ning, W. A novel non-enzymatic electrochemical glucose sensor modified with FeOOH nanowire. *Electrochem. Commun.* **2010**, *12*, 1581–1584. [[CrossRef](#)]

Disclaimer/Publisher's Note: The statements, opinions and data contained in all publications are solely those of the individual author(s) and contributor(s) and not of MDPI and/or the editor(s). MDPI and/or the editor(s) disclaim responsibility for any injury to people or property resulting from any ideas, methods, instructions or products referred to in the content.